Check for updates

Proceedings of the ASME 2021 Heat Transfer Summer Conference
HT2021
June 16-18, 2021, Virtual, Online

HT2021-62290

Downloaded from http://asmedigitalcollection.asme.org/HT/proceedings-pdf/HT2021/84874/V001T13A001/6734128/v001t13a001-ht2021-62290.pdf by Texas A & M University user on 30 August 2021

FEMTOSECOND TWO-PHOTON 3D LIGHTFIELD LITHOGRAPHY

Aravind Jakkinapalli
Texas A&M University
College Station, USA

Balaji Baskar
Texas A&M University
College Station, USA

Sy-Bor Wen *
Associate professor
Texas A&M University
College Station, USA

ABSTRACT

Based on the successful single-photon 3D light field photolithography we demonstrated in the last year, we extend the methodology to femtosecond 3D light field lithography. Compared with our previous single-photon work with UV LED light, using femtosecond light and the associated two-photon light absorption in 3D light field lithography can cure photoresist only around designed voxel locations in a 3D space. Such a two-photon scheme can prevent the unwilling curing of photoresists along the optical paths of rays before arriving at designed voxel locations, which is observed in our previous UV LED-based single-photon 3D light field lithography. The experimental scheme of femtosecond two-photon 3D light field lithography starts from delivering uniform femtosecond laser pulses to a spatial light modulator. The designed pixel map is presented on the spatial light modulator and then delivered to a microlens array to construct a 3D virtual image in the free space. By compressing the 3D virtual image in a photoresist layer with a microscope system, we can successfully generate different microscale 3D patterns without relying on scanning processes as in traditional 3D lithography. In this study, we present preliminary results of (a) algorithms developed to generated 3D patterns with femtosecond light, which should satisfy additional constraints when femtosecond light is used, and (b) 3D patterns generated in photoresists with femtosecond two-photon 3D light field lithography.

1. INTRODUCTION

The ever-growing competition amongst semiconductors industries to challenge Moore's law has led to the miniaturization of electrical and mechanical systems in the micro and nanoscale range. The integrated circuit chips, micro-electrical mechanical systems (MEMS), microelectronics, and micro biomedical devices are all manufactured with different fabrication methods that are being developed almost every day by researchers around the world [1-4]. 2D fabrication techniques have been significantly replaced by 3D techniques since 3D microstructures have a better weight- to performance ratio and improved mechanical and electrical properties [5, 6].

3D microfabrication involves layering different materials one over the other to produce a 3D structure at a microscopic scale. More often complex 3D structures are to be fabricated which makes the fabrication technique with the least fabrication time more ideal. In the case of stereolithography, the fabrication is done at a 2D level with a support structure to elevate the stage. Extending this to a 3D structure involves layer by layer scanning/projection which takes more time for fabrication [7, 8]. Selective laser sintering which is similar to stereolithography also requires an elevator to selectively sinter the freshly coated material across the cross-section of the 3D structure to be fabricated [9]. In the case of holographic lithography with highly temporal coherent light, the fabrication time is improved significantly compared to the above-mentioned methods since the entire 3D structure can be patterned without the scanning or lifting stage. However, the holograms generated contain speckles due to which the spatial resolution of the fabricated 3D structure is reduced [10].

In the case of multiphoton lithography, the focal point of a coherent light source like lasers causes polymerization in the photoresists which drastically changes the solubility of the resist during the development process. This two-photon polymerization occurs at a single spot which makes the scanning process to fabricate complicated 3D structures very time-consuming [11, 12]. The fabrication time was reduced when single spot multiphoton lithography was replaced by multi-spot parallel processing lithography, however, this is limited to only periodic structures [13].

To have a throughput fabrication of complex structures, 3D light field photolithography technique is adopted in this study. This technique uses the inverse of light field imaging process in cameras where the intensity and direction of rays emanating

Copyright © 2021 by ASME

from an object are captured. A 3D structure can be reconstructed and fabricated in a single projection using this technique, thus eliminating the need for scanning and elevating stages [14]. As in conventional light field cameras, a microlens array (MLA) is used along with a spatial light modulator (SLM) to reconstruct a 3D image [15]. The intensity of light coming from each pixel of the SLM is chosen as a function of the voxels that have to be generated in 3D space using the MLA. With an accurate correspondence between SLM and MLA positions, all these voxels combine to form a virtual 3D structure in space. For fabrication in the microscale range, the 3D structure is further optically compressed by a telecentric lens pair and is patterned on a photoresist [16, 17]. Unlike holographic lithography, incoherent light sources such as UV light can be used for lithography and do not form unwilling speckles. However, UV LED light is not completely transparent to photoresist like lasers, which leads to unwanted curing along the optical path in the photoresist. This study uses femtosecond light and associated two-photon curing of photoresists at desired voxel locations and to improve the overall quality of fabrication.

In the following sections, we will describe our experimental setup, results, and data analysis of femtosecond two-photon light field photolithography

2. EXPERIMENTAL PROCEDURE

2.1. Setup

A ~14 femtosecond laser beam (~520 nm) of beam width ~1 cm diameter is first expanded by guiding it through a telecentric lens pair providing six times of magnification. This expansion facilitates the selection of a region from the beam with a uniform intensity profile. The expansion ratio is selected to have a highly uniform region around the center of the expanded beam and sufficient light intensity to cure photoresists with two-photon polymerization (TPP) at each of the generated voxels from 3D light field projection. The uniform beam after the expansion is delivered to the Spatial Light Modulator (SLM) consisting of a digital Mirror Device (DMD) which can be programmed to either activate or deactivate each pixel. The following set up in figure 1 remains unchanged from the single-photon 3D light field projection and consists of a telecentric lens pair with an iris at the 1 focal distance (i.e., 1 f) location as an optical relay to deliver a parallel virtual SLM image at the output as illustrated. The Micro Lens Array (MLA) is placed at a distance of 1.1 f_MLA away from the SLM imaging plane, where f_MLA is the focal length of the MLA (~4.8 mm). The 3-D projection is further compressed using a second telecentric system consisting of a 200 mm tube lens and a 16x objective lens. A beam splitter is placed before the objective lens to direct light to a camera for inspection.

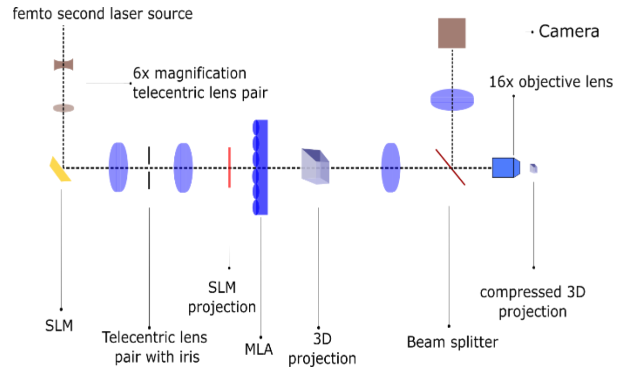

FIGURE 1: SCHEMATIC OF THE EXPERIMENTAL SETUP FOR FEMTOSECOND 3D LIGHTFIELD TWO-PHOTON PHOTOLITHOGRAPHY

2.2. SLM – MLA calibration

The accuracy of the 3D object reconstruction using the proposed 3D light field projection relies on an accurate determination of relative positions of the MLA and SLM. For every voxel that constitutes the virtual 3D object, the corresponding microlens and pixel on the SLM to be utilized in the projection are determined with ray-tracing methods. The ray-tracing method assumes that light travels parallel to the optical axis from SLM to MLA to determine the pixels on the SLM to be turned on. Hence a one to one correspondence between the SLM and MLA is required for performing the experiments.

The calibration procedure was done in two methods, *Method 1* - By calibrating both SLM and MLA together with respect to the camera, *Method 2* - By calibrating SLM and MLA individually with respect to the camera and correlating the data.

2.2.1. Method 1

The projector, telecentric lens pair, MLA, and camera were aligned along the same optical axis with a solid field image generated with the SLM as shown in figure 2. The solid field image was then loaded into a Matlab code to run a zeroth iteration of the calibration procedure. The zeroth iteration involves approximate identification of the MLA boundaries from the solid field image. Once the boundaries were identified, the first iteration of the calibration procedure was run where the position of maximum intensity on each boundary was determined using a test line perpendicular to the boundary. The intensity values were checked along these test lines and the position of max intensity was identified as shown in figure 3. It was observed that a larger width of these test lines can improve the accuracy of the boundary detection.

The next iteration step (second iteration) in the calibration procedure is unique to this method, where the relative position between the SLM and MLA is calibrated. This iteration involves projecting and capturing horizontal boundary line images and vertical boundary line images separately and checking for

Downloaded from http://asmedigitalcollection.asme.org/HT/proceedings-pdf/HT2021/84874/V001T13A001/6734128/v001t13a001-ht2021-62290.pdf by Texas A & M University user on 30 August 2021

Copyright © 2021 by ASME

intensity value at the positions determined in iteration 1. The maximum intensity in the captured image indicates the projected SLM lines overlap the boundaries of the MLA. The number of boundary line images (vertical/horizontal) depends on the degree of accuracy with which we need to calibrate the SLM and MLA. As a good practice, 13 images for horizontal boundary lines and 13 images for vertical boundary lines were used with 1 and 13 being on two extreme positions. The sequence of this method is illustrated as a flow chart in figure 4a.

FIGURE 2: SOLID FIELD IMAGE OF MLA AND SLM CAPTURED ON CAMERA

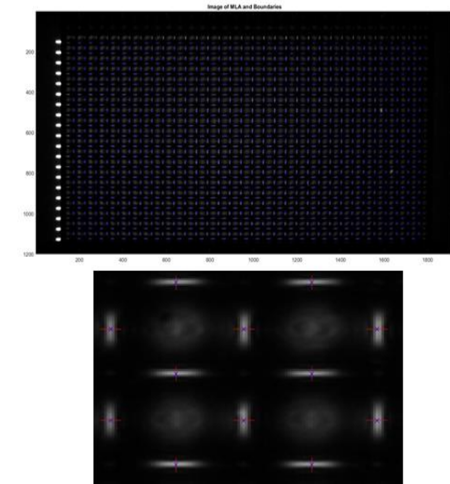

FIGURE 3: INTENSITY CHECK ON BOUNDARIES USING TESTLINES

2.2.2. Method 2

This second method divides the calibration into two parts. First, the MLA is removed from the setup and the SLM pixel positions on the camera are calibrated using a blue dotted grid image as shown in figure 5. Then the MLA is added back to the setup. A solid field image was then loaded into a Matlab code to determine the MLA boundaries from the solid field image. The sequence of this method is illustrated as a flow chart in figure 4b. This second calibration method is much faster than the first method. Moreover, this second method contains fewer possible calibration errors. It was found that 3D objects are better projected after the second calibration method.

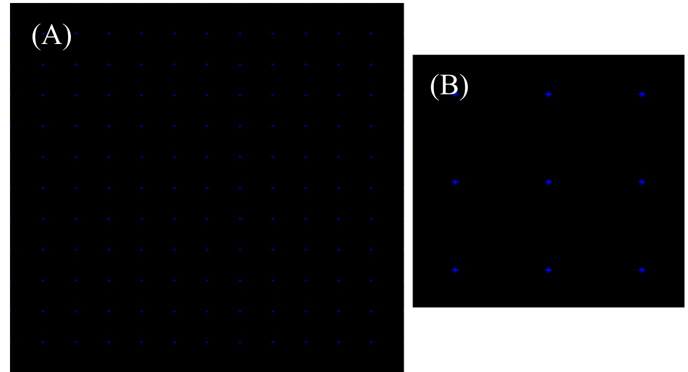

FIGURE 4: (A) BLUE DOTTED GRID IMAGE FOR SLM CALIBRATION IN METHOD 2 (B) ZOOMED IMAGE OF GRID SHOWING INDIVIDUAL DOTS

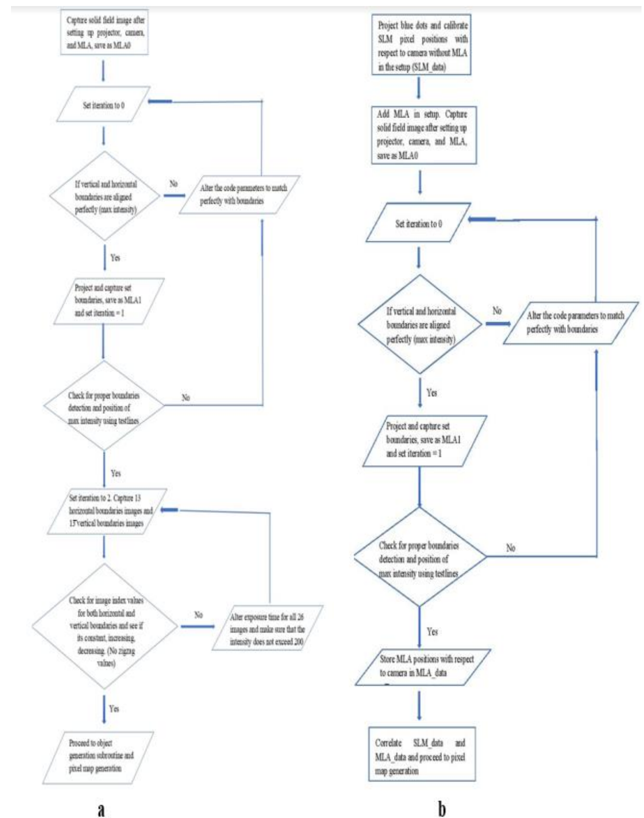

FIGURE 5: FLOW CHART OF STEPS INVOLVED IN SLM-MLA CALIBRATION USING (A) METHOD 1 (B) METHOD 2

Downloaded from http://asmedigitalcollection.asme.org/HT/proceedings-pdf/HT2021/84874/V001T13A001/6734128/v001t13a001-ht2021-62290.pdf by Texas A & M University user on 30 August 2021

Copyright © 2021 by ASME

2.3. Pixel mapping algorithm

After the calibration of the SLM pixels with the position of the MLA and the camera, we can program the SLM to switch on the relevant pixels to project a voxel of our choosing. The algorithm used for the single-photon 3D lithography involved discretizing the 3D structure into multiple voxels. The SLM pixels responsible for the generation of the voxels were identified using ray optics and the appropriate pixel value map was generated for each pattern. This algorithm does not account for the unwilling intersection of light rays occurring at locations that are not intended to be cured. It is also imperative that the rays intersecting at the desired voxel arrive within a time interval that is lesser than the pulse duration to facilitate the TPP. To overcome these limitations, a new algorithm is developed for the femtosecond pulses. The procedure to identify the active MLA for each voxel remains unchanged. As illustrated in figure 6, it is clear that using specific symmetric locations with respect to the MLA structure provides a good foundation to ensure that the rays are symmetric and devoid of a path difference. Identifying these path differences is a crucial step in our TPP lithography (the pixel value map generation). The first step in the pixel value map generation algorithm is to identify the symmetric locations. Two such candidates are observed, namely, (1) center positions, and (2) symmetric positions. Center positions are those positions that are located at the center of an MLA. Symmetric positions are those positions that are located at the center of a 2X2 array of MLA. Irrespective of their z location beyond a certain threshold, both these positions can host voxels whose constituent rays are symmetric. The center and symmetric positions are illustrated in figure 7.

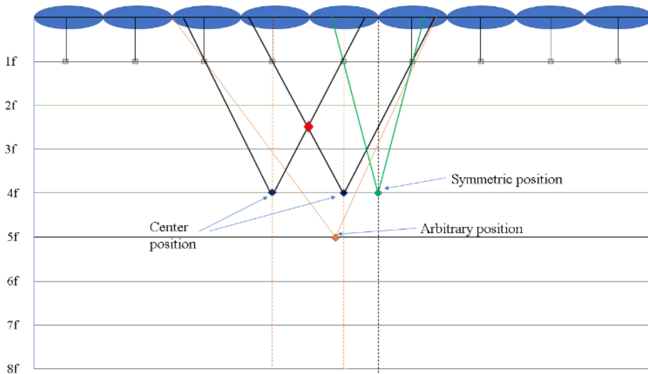

FIGURE 6: VOXEL LOCATIONS AND THEIR CORRESPONDING RAY INTERSECTIONS.THE SYMMETRIC AND CNETER POSITIONS HAVE RAYS WITH NO PATH DIFFERENCE

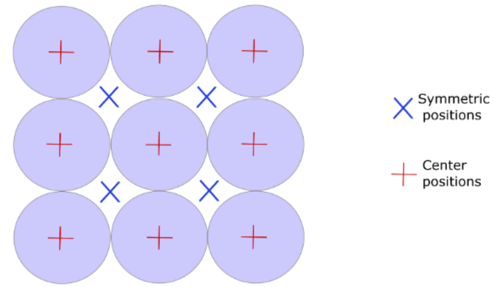

FIGURE 7: MICROLENS ARRAY ILLUSTRATION WITH THE SYMMETRIC AND CENTER VOXEL POSITIONS

The 3D structures can be generated by selecting the voxels which lie in the interior of the structure and correspond to the symmetric positions as described. As illustrated in figure 6 by the red diamond, the generation of 2 symmetric location voxels at a given depth using 2 rays for each voxel causes the unwilling curing at a third position. Following the selection of the voxels, another algorithm is applied to prevent the unwilling curing of the resist at undesirable locations. The minimum number of rays required to cure the photoresist at the voxel is identified. The rays responsible for the generation of each voxel are identified using the pixel selection scheme[18]. The total number of rays available for each voxel varies as a function of the depth of the voxel with more rays available at larger depths as shown in table 1.

Depth/f	Rays	Depth/f	Rays
3	0	11	60
4	4	12	60
5	8	13	88
6	20	14	100
7	20	15	114
8	29	16	124
9	39	17	148
10	44	18	164

TABLE 1: NO OF RAYS AVAILABLE FOR EACH VOXEL AT VARIOUS DEPTHS

Rays intended for different voxels might intersect with each other if their path difference at the point of intersection is less than the distance traveled by the propagation distance of ~14 fs light during each laser pulse. In the event of the intersection of rays, the ray is assigned to the voxel with the fewer total rays. This assignment algorithm can reduce the number of intersection points and thus prevent unwanted curing of the photoresist. The

Downloaded from http://asmedigitalcollection.asme.org/HT/proceedings-pdf/HT2021/84874/V001T13A001/6734128/v001t13a001-ht2021-62290.pdf by Texas A & M University user on 30 August 2021

Copyright © 2021 by ASME

equation for the z resolution at a particular depth of projection z is as follows where i is the MLA lenslet index with respect to the voxel, D is the diameter of the lens, f is the focal length of the MLA, z is the depth of the voxel from the plane of the MLA and s is the DMD pixel size.

$$\frac{(4iDfs(z-f)^2)}{(2iDf)^2 - s^2(z-f)^2} * 0.5$$

The minimum separation distance between two layers should be greater than the depth resolution at that layer to ensure that both the voxels are generated individually. With these restrictions on the x, y, and z positions of the voxels we can generate the pixel value map for the 3D structures of our choosing. The pixel value maps and 3D voxel maps using the old and new algorithm for a vertical wall of uniform cross-sections are shown in figure 8. The old algorithm selects voxels based on the separation distance specified. The periodic separation of the voxels in a layer can be made arbitrary and the layer separation did not have any restrictions in the old scheme. The new algorithm selects the symmetric voxels and has a constant periodicity in a layer for a specific MLA. The layer separation varies as a function of the layer depth as explained in the previous section.

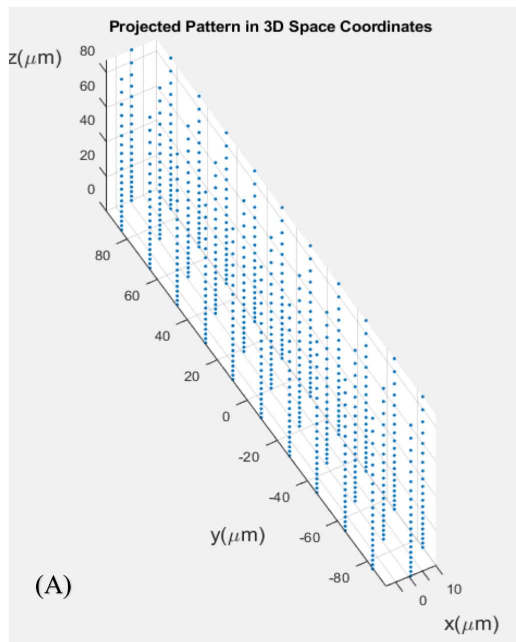

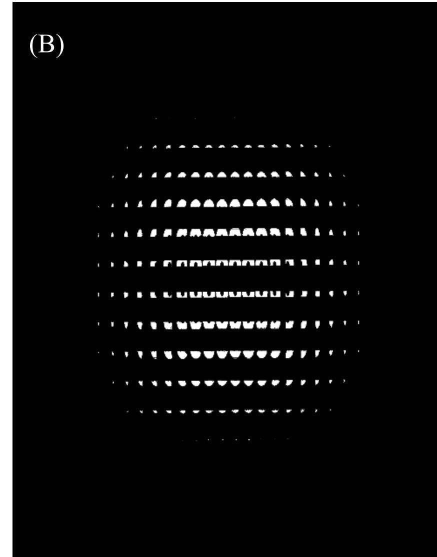

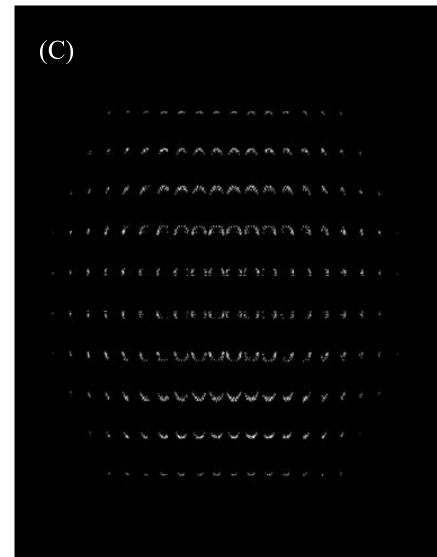

FIGURE 8: (A) 3-D VOXEL MAP OF THE VERTCAL WALL STRUCTURE CONSTRUCTED WITH THE SYMMETRIC AND CENTER POSITIONS. (B) PIXEL VALUE MAP OF THE VERTICAL WALL GENERATED WITH DENSE VOXELS. (C) PIXEL VALUE MAP OF THE VERTICAL WALL GENERATED USING THE RAY SELECTION ALGORITHM

3. RESULTS AND DISCUSSIONS

The proposed algorithm is applied to the generation of a vertical wall of height 120 microns after compression. The 3D patterns are formed from 6f to 12f in front of the MLA to have a relatively uniform z-resolution [17]. The compressed 3D patterns are delivered to the SU-8 photoresist. To ensure consistent experimental conditions for the projections, the laser energy is measured and verified to be above 7 mW. The SU-8 sample is loaded onto the sample holder and held firmly using a double-sided tape. The sample holder is equipped with translational stages in the x,y, and z directions to help place the sample at the required projection position. The sample loading could introduce a slight tilt that causes a mismatch in the perceived and the actual depth of our pattern projections when multiple patterns are

Downloaded from http://asmedigitalcollection.asme.org/HT/proceedings-pdf/HT2021/84874/V001T13A001/6734128/v001t13a001-ht2021-62290.pdf by Texas A & M University user on 30 August 2021

Copyright © 2021 by ASME

projected on the same sample at different positions. To prevent this, the left and the right edges of the photoresist sample are cleaned with a swab dipped in acetone to reveal the silicon surface, onto which the patterns are projected. The z position of the sample holder is adjusted using the translation stage and recorded when the sample pattern is observed to be at the silicon surface on the camera. By repeating the process at the other end of the sample, the required z position at any intermediate location on the sample can be interpolated.

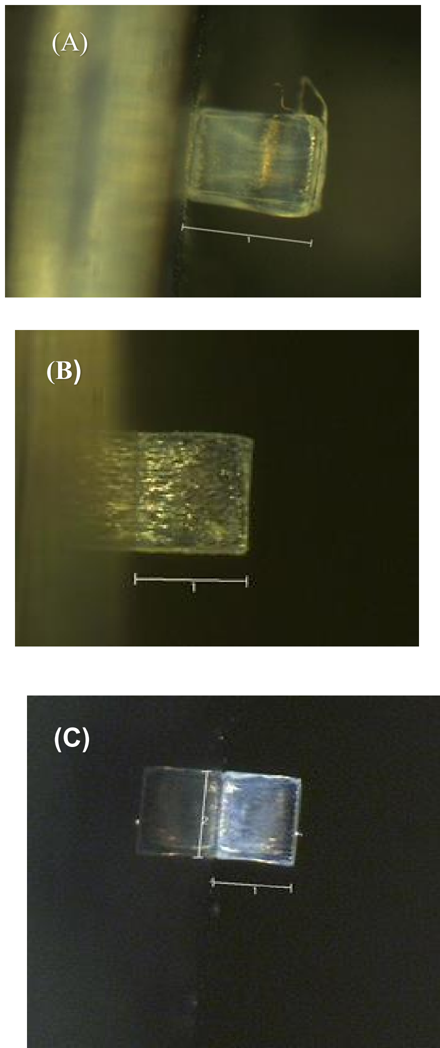

FIGURE 9: DEVELOPED PATTERNS FOR (A) PATTERNS WITH DENSELY PACKED VOXELS WITH ALL RAYS THE PATTERN HEIGHT IS 386 MICRONS (B) PATTERNS WITH SYMMETRIC AND CENTER VOXELS WITH ALL RAYS. THE PATTERN HEIGHT IS 212 MICRONS, (C) PATTERNS WITH SYMMETRIC AND CENTER VOXELS WITH REDUCED RAYS. THE PATTERN HEIGHT IS 173 MICRONS

Using the projection at the silicon surface as a reference, the sample is translated in both the positive and negative directions to identify the depth at which the developed patterns are completely retained. The patterns are then projected at this depth. The photoresist sample is prepared by spin coating SU-8 2150 on the back surface of a silicon wafer at a spin speed of 1750 rpm for 1 minute, followed by a 60 minute preheat at 90 °C. The exposed sample is then heated for 30 minutes at 90 °C before immersing the sample in a SU-8 developer for a further 30 minutes. Figure 9 shows the developed samples for various patterning conditions.

Figure 9a shows the pattern generated using the dense voxel separation causing unwilling curing above the structure. Figures 9b and 9c are obtained by spacing the voxels at the center and symmetric positions with all rays and reduced rays utilized for curing the resist respectively. These patterns are uniform. As expected, the patterns generated with a high voxel density show additional patterns due to unwilling curing. The patterns generated with the center and symmetric voxels have a more uniform structure. The patterns generated with the ray selection algorithm could not yield stable free-standing structures and we expect to obtain results closest to the design patterns once we tweak the exposure conditions for these structures.

Figures 9a, 9b, and 9c show 266 microns, 92 microns, and 53 microns height deviation respectively from the designed height of 120 microns. The differences between the pattern shapes and height after the development, compared to the design patterns can be attributed to the following reasons.

1. Weak patterns after development possibly due to low voxel density - the current voxel period for a given layer depth is dictated by the dimension of the MLA. We do not have the freedom to space the voxels any closer than they currently are. Using a high-resolution lateral translation stage for the sample in the future, we will be able to manually move the sample by a distance equal to half the voxel separation and project the same pattern to increase the voxel density in one direction. Alternatively, using an MLA with a smaller lens diameter (smaller NA) can also increase the voxel density.
2. Additional structures atop the design pattern due to unwilling curing of the resist- As explained earlier, rays intended for a particular set of voxels might cure the photoresist at undesired locations. The current algorithm can be further improved to remove any unwilling curing except at the 1 f location.
3. Mismatched height between the design and the developed pattern. The z resolution is a function of the layer depth (eq1) The ray selection algorithm works better with the availability of a larger number of active MLA for a given voxel. This is observed in higher layer depths. The competing nature of the ray selection algorithm vs high z resolution limits the generation of uniform patterns of the designed height.

Downloaded from http://asmedigitalcollection.asme.org/HT/proceedings-pdf/HT2021/84874/V001T13A001/6734128/v001t13a001-ht2021-62290.pdf by Texas A & M University user on 30 August 2021

Copyright © 2021 by ASME

4. SUMMARY

In this technical work, we have presented the preliminary results of femtosecond two-photon lithography using 3D light field projection. A new algorithm for calibrating the relative positions of SLM and MLA is proposed and compared with our older algorithm. Our older pixel mapping algorithm of selecting arbitrary voxels based on separation distance is modified and replaced by a newer algorithm that prevents unwanted curing of the photoresist at positions different from the desired voxel position by considering the positions of voxels with respect to the MLA (center and symmetric). The layer separation was also updated to account for the varying resolution along the z-direction. The proposed method can be used in fabricating complex computer-designed 3D structures in a single projection quickly without scanning. The future research aims at ideally zero deviation between fabricated and design pattern by improving the algorithm to space out voxels in a way that the rays with the same optical path do not intersect at all. This involves a specific selection of ray angles and active microlens for each voxel relative to other voxels in the vicinity. By using this approach, the unwilling curing at all z locations can be eliminated to achieve high precision 3D photolithography.

ACKNOWLEDGEMENTS

The research is support by the National Science Foundation (CMMI-1826078). The authors like to appreciate technical supports from Dr. Yakovlev's group at TAMU.

REFERENCES

[1] Waits, C. M., Morgan, B., Kastantin, M., and Ghodssi, R., 2005, "Microfabrication of 3D silicon MEMS structures using gray-scale lithography and deep reactive ion etching," Sensors and Actuators A: Physical, 119(1), pp. 245-253.

[2] SUZUMORI, K., KOGA, A., and HANEDA, R., 1994, "Microfabrication of Integrated FMAs using Stereo Lithography," Proceedings IEEE Micro Electro Mechanical Systems An Investigation of Micro Structures, IEEE, Oiso, Japan, Japan.

[3] A.Bertsch, H.Lorenz, and P.Renaud, 1999, "3D microfabrication by combining microstereolithography and thick resist UV lithography," Sensors and Actuators A: Physical, 73(1-2), pp. 14-23.

[4] Yoon, Y. K., Park, J. H., and Allen, M. G., 2006, "Multidirectional UV Lithography for Complex 3-D MEMS Structures," J Microelectromech S, 15(5), pp. 1121-1130.

[5] Han, M., Lee, W., Lee, S.-K., and Lee, S. S., 2004, "3D microfabrication with inclined/rotated UV lithography," Sensors and Actuators A: Physical, 111(1), pp. 14-20.

[6] Otter, W. J., and Lucyszyn, S., 2016, "3-D printing of microwave components for 21st century applications," IEEE MTT-S International Microwave Workshop Series on Advanced Materials and Processes for RF and THz Applications (IMWS-AMP), IEEE, Chengdu.

[7] Bertsch, A., Jiguet, S., and Renaud, P., 2004, "Microfabrication of ceramic components by microstereolithography," Journal of Micromechanics and Microengineering, 14(2), pp. 197-203.

[8] Gauvin, R., Chen, Y. C., Lee, J. W., Soman, P., Zorlutuna, P., Nichol, J. W., Bae, H., Chen, S., and Khademhosseini, A., 2012, "Microfabrication of complex porous tissue engineering scaffolds using 3D projection stereolithography," Biomaterials, 33(15), pp. 3824-3834.

[9] Fina, F., Goyanes, A., Gaisford, S., and Basit, A. W., 2017, "Selective laser sintering (SLS) 3D printing of medicines," Int J Pharm, 529(1-2), pp. 285-293.

[10] Kondo, T., Juodkazis, S., Mizeikis, V., Misawa, H., and Matsuo, S., 2006, "Holographic lithography of periodic twoand three-dimensional microstructures in photoresist SU-8," Optics Express, 14(17), pp. 7943-7953.

[11] Jhaveri, S. J., McMullen, J. D., Sijbesma, R., Tan, L.-S., Zipfel, W., and Ober, C. K., 2009, "Direct Three-Dimensional Microfabrication of Hydrogels via Two-Photon Lithography in Aqueous Solution," Chem Mater, 21(10), pp. 2003-2006.

[12] Seokwoo Jeon, V. M., John A. Rogers, and Gary P. Wiederrecht, 2006, "Fabricating three dimensional nanostructures using two photon lithography in a single exposure step," Optics Express, 14(6), pp. 2300-2308.

[13] Ritschdorff, E. T., Nielson, R., and Shear, J. B., 2012, "Multi-focal multiphoton lithography," Lab Chip, 12(5), pp. 867-871.

[14] Martínez-Corral, M., and Javidi, B., 2018, "Fundamentals of 3D imaging and displays: a tutorial on integral imaging, light-field, and plenoptic systems," Advances in Optics and Photonics, 10(3).

[15] Arai, J., Kawai, H., and Okano, F., 2006, "Microlens arrays for integral imaging system," Appl Optics, 45(36), pp. 9066-9078.

[16] Zhang, H., Wen, S.-B., Unger, B. L., and DeGroote Nelson, J., 2019, "Microlens array based three-dimensional light field projection and possible applications in photolithography," Optifab 2019.

[17] Zhang, H., and Wen, S. B., 2020, "3D photolithography through light field projections," Appl Opt, 59(27), pp. 8071-8076.

[18] Zhang, S.-B. W. H., 2020, "3D LIGHT FIELD PROJECTION AND THE ASSOCIATE 3D PHOTOLITHOGRAPHY," ASME 2020 Heat Transfer Summer Conference.

Downloaded from http://asmedigitalcollection.asme.org/HT/proceedings-pdf/HT2021/84874/V001T13A001/6734128/v001t13a001-ht2021-62290.pdf by Texas A & M University user on 30 August 2021

Copyright © 2021 by ASME